Electrically tunable spin qubits in strain-engineered graphene p-n junctions

Myung-Chul Jung *[1,2] and Nojoon Myoung †[1,2]

[1]Department of Physics Education, Chosun University, Gwangju 61452, Republic of Korea
[2]Institute of Well-Aging Medicare & Chosun University G-LAMP Project Group, Chosun University, Gwangju 61452, Republic of Korea

---

*first author: `mcjung24@chosun.ac.kr`
†Corresponding author: `nmyoung@chosun.ac.kr`

Supplementary Materials Section 1. Snake-like trajectory

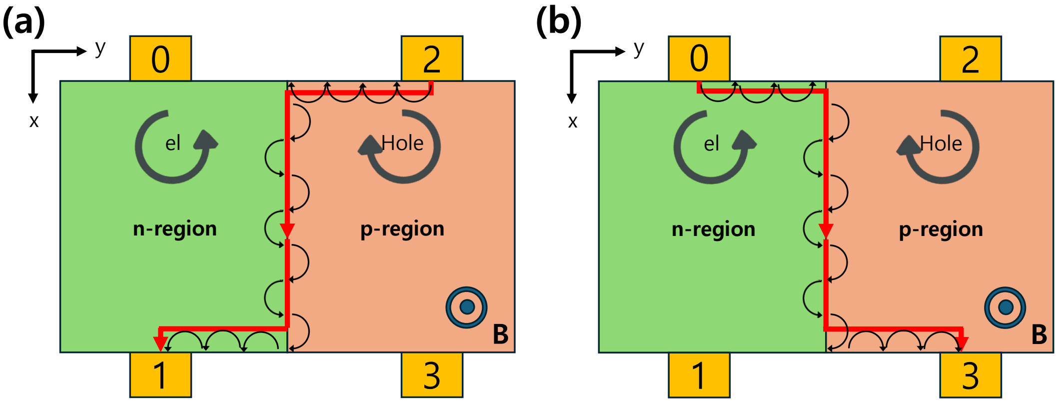

Figure S1: Schematic illustration of current trajectory in a *p*-*n* junction under a homogeneous perpendicular magnetic field. The panels (a) and (b) show possible configurations of quantum Hall edge channels along the junction interface. Electrons in the *n*-region and holes in the *p*-region propagate along chiral trajectories, forming snake-like states at the junction. The red arrows indicate representative current paths.

The formation of such trajectories at a graphene *p*-*n* junction under a perpendicular magnetic field originates from the opposite cyclotron motion of electrons and holes. In the *n*-region, electrons undergo cyclotron motion in one direction (e.g., counterclockwise), whereas in the *p*-region, holes bend in the opposite direction (clockwise), as illustrated in Supplementary Fig. S1. As a result, carriers crossing the interface experience alternating curvature, giving rise to snake-like trajectories that propagate along the junction.

In our system, we consider an antisymmetric *p*-*n* junction with opposite Chern numbers in the two regions [1]. In this case, the semiclassical picture naturally supports the formation of snake-like interface modes. These modes correspond to the transport path from lead 2 to lead 1, as shown in Supplementary Fig. S1(a), which is consistent with Fig. 1(a) in the main text. The corresponding transport path from the *n*-region to the *p*-region is illustrated in Supplementary Fig. S1(b). Importantly, when transport is considered in the opposite direction (from lead 0 to lead 3), the system exhibits qualitatively identical behavior, confirming the robustness of the snake-state transport.

Supplementary Materials Section 2. Quantum conductance and Fano resonance line

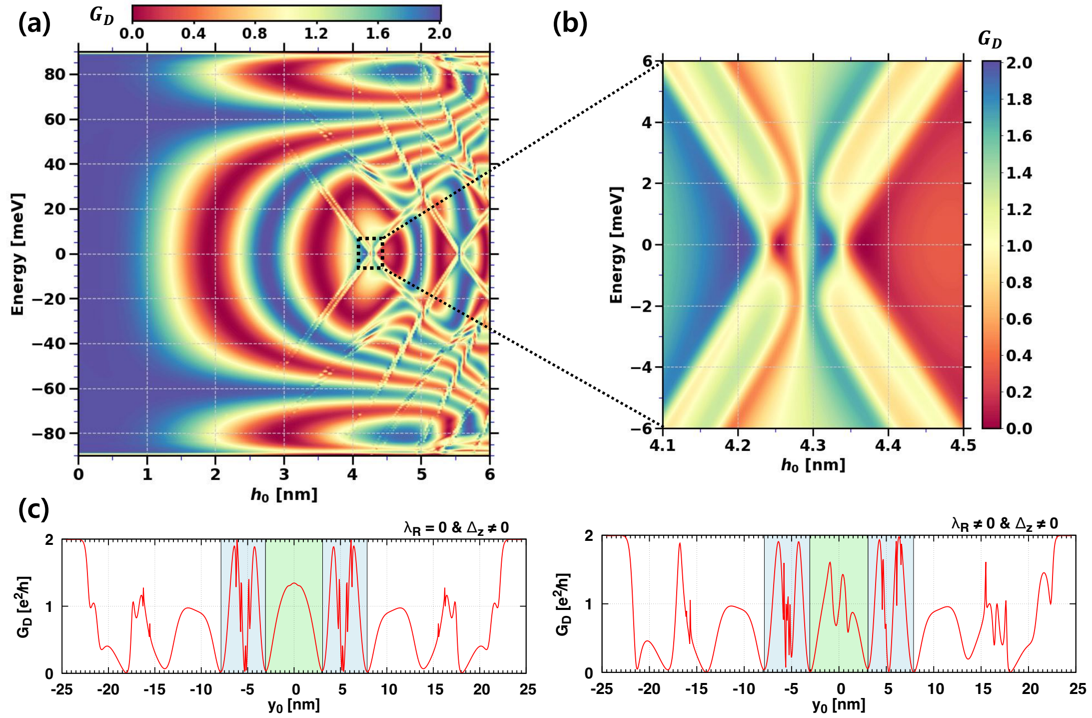

Figure S2: Quantum conductance map and quantum conductance linecut at $h_0 = 4.3\ nm$. (a) Quantum conductance under only the Zeeman field ($1.7\ meV$) without RSOC. (b) The zoomed-in views around the single quantum dot (SQD) ground level in the range of $h_0 = 4.1$ to 4.5 nm. (c,d) Quantum conductance line as a function of y_0 for Zeeman coupling only (c) and for both RSOC ($10.1\ meV$) and Zeeman coupling (d).

Figure S2(a) shows the conductance resonances without Rashba spin-orbit coupling (RSOC) in the quantum conductance G_D characteristics of the strained graphene system, which are analogous to a spinful counterpart of those observed in the charge qubit system [2, 3]. In the absence of RSOC, the Zeeman field produces two distinct spin-split branches, leading to independent crossing Fano resonance lines. In contrast, when RSOC is taken into account, the spin-orbit interaction mixes the spin states. The inclusion of RSOC modifies the conductance resonances in the strained graphene qubit system, as shown in Fig. 2(a) of the main text. The zoomed-in regions around the single quantum dot (SQD) regime are highlighted in Supplementary Fig. S2(b) for the case without RSOC, which clearly exhibit the gap evolution near the ground-state level.

Supplementary Figures S2(c) and S2(d) display the line cuts of the quantum conductance G_D as a function of the interface channel position y_0 for h_0=4.3 nm. Supplementary Figure S2(c) considers Zeeman coupling only, while Supplementary Fig. S2(d) includes both RSOC and Zeeman coupling. Also, G_D with RSOC clearly shows an asymmetric shape. The green area is the SQD activation region and the blue area is the DQD activation region, as shown in the main text, respectively.

Supplementary Materials Section 3. Scalable tight-binding model

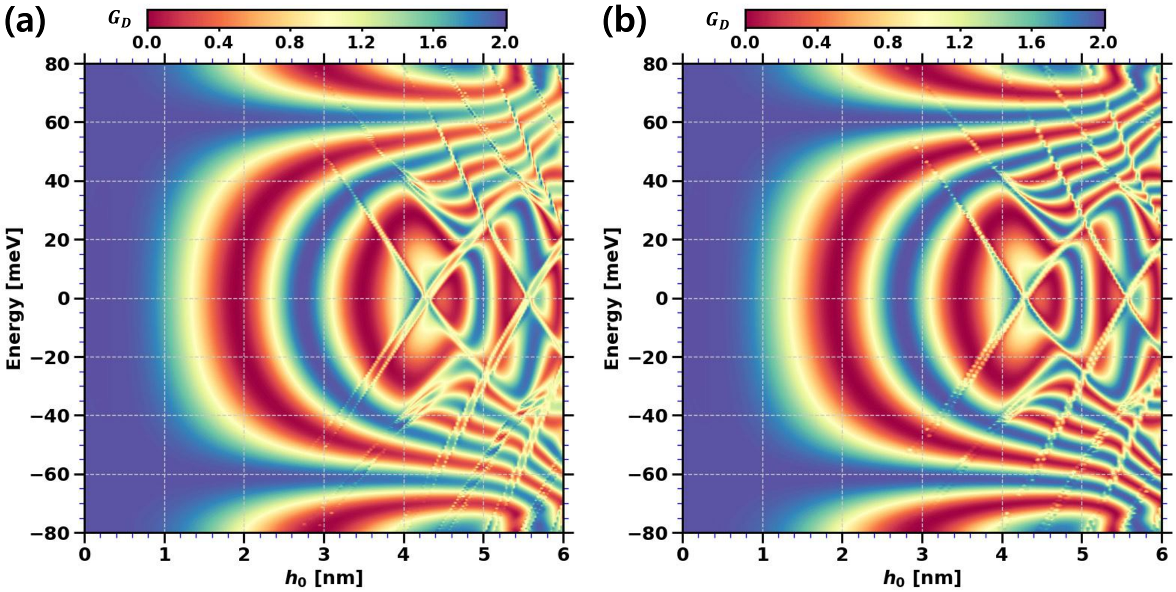

Figure S3: Quantum conductance G_D maps as a function of energy and nanobubble height h_0. The map for the original system (a) and a scaled system (b) for $\lambda_R = 10.1\ meV$ and $\Delta_z = 1.7\ meV$.

In the present calculations, a relatively large external magnetic field ($B_z \sim 30\ T$) is employed. This choice originates from the limited system size accessible in our numerical simulations, where the magnetic length and the confinement length scale are intrinsically linked. As a result, smaller simulated devices require larger magnetic fields to reproduce the same quantum Hall–assisted confinement physics.

Importantly, this does not imply that the proposed qubit mechanism intrinsically requires such high magnetic fields. For larger device sizes, the same physical regime can be achieved at proportionally smaller B_z. This scaling behavior is consistent with recent studies [4, 5] on strained graphene systems, where an efficient scaling approach has been demonstrated. Following this idea, we apply the transformation $a \to sa$, $t \to t/s$, $u \to su$, $h \to \sqrt{s}h$, and confirm that for scaling factor $s = 2$, essentially identical results are obtained with a reduced magnetic field of $B_z \sim 7.5\ T$.

These results indicate that the large magnetic field used in this work should be understood as a computational constraint rather than a fundamental requirement. Therefore, the spin-qubit behavior predicted here is expected to be realizable under more experimentally accessible magnetic fields in appropriately scaled strained-graphene devices.

Supplementary Materials Section 4. Detuning energy versus RSOC

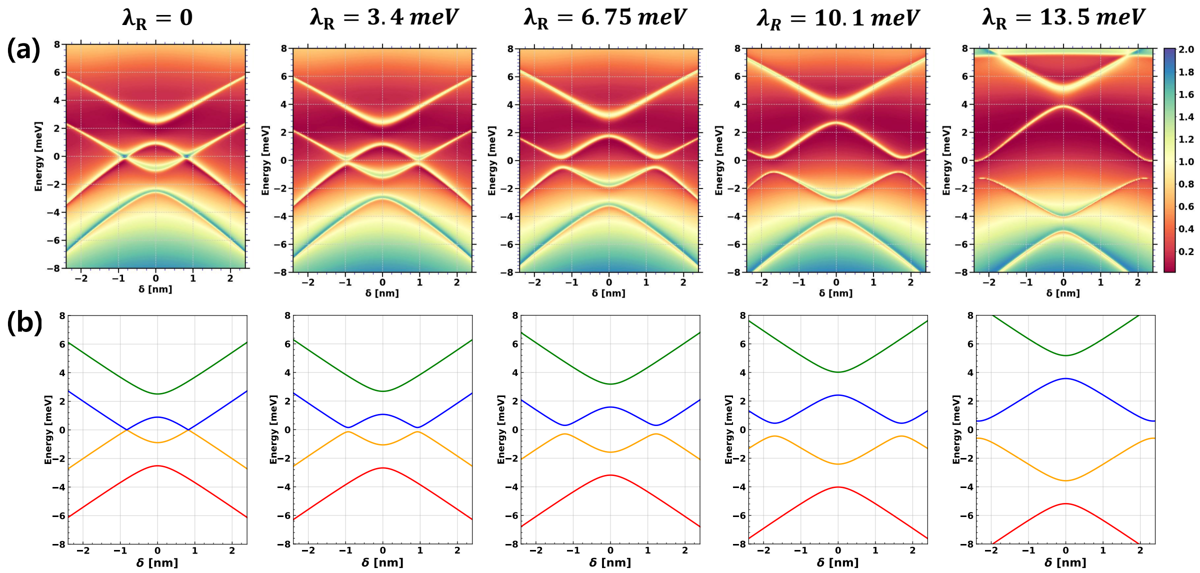

Figure S4: Detuning energy spectra as a function of λ_R. (a) Numerical detuning spectra obtained from tight-binding simulations. (b) Analytical detuning spectra calculated using the four-band Hamiltonian model.

To clarify the role of RSOC in the energy spectrum as a function of detuning, we systematically investigated the energy spectral evolution by varying the RSOC strength under a fixed Zeeman splitting $\Delta_z = 1.7\ meV$. Supplementary Figure S4(a) presents the calculated energy spectra for increasing RSOC strengths ranging from $\lambda_R = 0$ to $13.5\ meV$.

In the absence of RSOC ($\lambda_R = 0$), a finite spin-conserving gap is present, while the spin-flip gap remains closed. Upon introducing a finite RSOC, the spin-conserving gap is gradually reduced, reflecting a reshaping of the effective DQD confinement potential and a redistribution of electronic probability density between the two dots induced by RSOC (see Supplementary Materials Section 6 for details). In contrast, the spin-flip gap increases approximately linearly with RSOC strength, as shown in Supplementary Fig. S6(a).

The linewidth of each energy level is related to the spin relaxation time T_1, following an inverse relation $\Gamma \propto 1/T_1$. As the RSOC strength increases, the linewidth associated with the upper spin-conserving branch becomes broader, indicating a reduction of the relaxation time due to enhanced spin-orbit-induced relaxation. Conversely, the linewidth of the spin-flip branch becomes progressively sharper, corresponding to a longer relaxation time.

We additionally analyzed the detuning spectrum using an effective four-band Hamiltonian model. The analytical results shown in Fig. S4(b) are fully consistent with our numerical simulations.

Overall, RSOC provides a highly tunable mechanism to activate and control the detuning-induced spin hybridization. The progressive opening of the avoided crossing gap with increasing λ_R establishes a direct link between RSOC strength, effective potential deformation, modification of the wavefunction overlap, and the emergence of electrically driven spin-flip Rabi dynamics, as experimentally probed and discussed in the main text.

Supplementary Materials Section 5. Eigenstates and current density of detuning spectrum

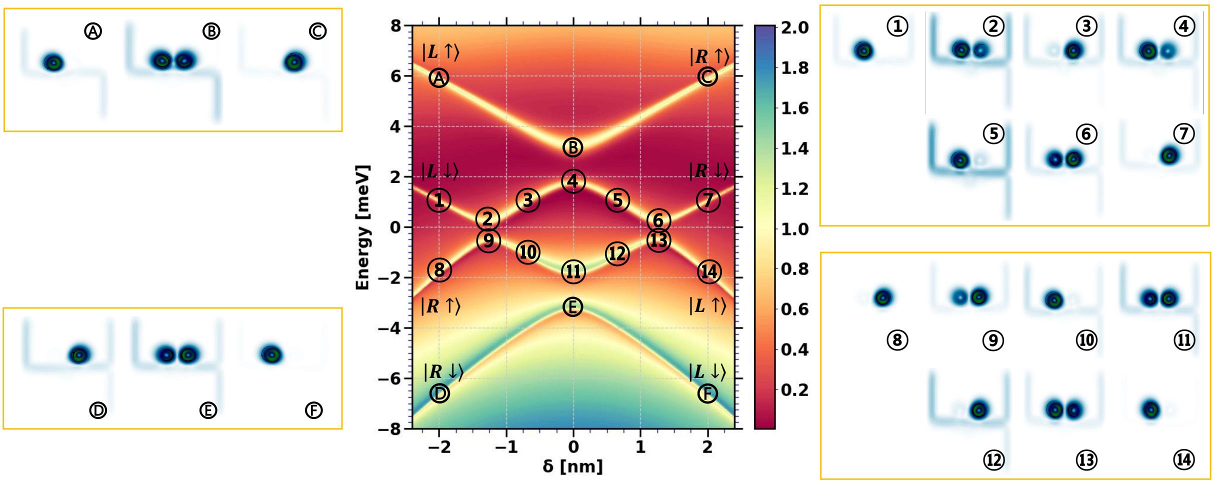

Figure S5: Detuning-dependent energy spectrum and spatial localization of the eigenstates ($\lambda_R = 6.75\ meV$ and $\Delta_z = 1.7\ meV$). Central panel: Energy spectrum of the double quantum dot as a function of detuning δ, showing the four hybridized states labeled as $|L\uparrow\rangle$, $|L\downarrow\rangle$, $|R\uparrow\rangle$, and $|R\downarrow\rangle$. The colored circles mark the eigenenergies at selected detuning values. Left and right panels: Current density corresponding to the numbers and alphabet labels in the central spectrum.

Supplementary Figure S5 illustrates the detuning energy spectrum of the graphene DQDs, displaying the four relevant eigenvalues. Each colored circle represents the current density of the corresponding eigenstate evaluated at a specific energy and detuning value, providing a direct visualization of the real-space localization and hybridization of the quantum states (without explicitly showing spin states).

The left and right quantum dots are denoted as $|L\rangle$ and $|R\rangle$, respectively. From top to bottom, the four eigenstates are labeled as $|L\uparrow\rangle$, $|L\downarrow\rangle$, $|R\uparrow\rangle$, and $|R\downarrow\rangle$, corresponding to the spin-resolved localized states of each dot.

As shown in Supplementary Fig. S5, near the avoided crossing point the eigenstates hybridize into superposed states across the two dots, leading to spatial delocalization of the wavefunctions. At zero detuning ($\delta = 0$), the superposition occurs between states with the same spin orientation, resulting in bonding and antibonding superpositions of the form

$$|\psi\rangle_{upper} = \frac{1}{\sqrt{2}}\left(|L,\uparrow\rangle \pm |R,\uparrow\rangle\right), \quad \text{or} \quad |\psi\rangle_{lower} = \frac{1}{\sqrt{2}}\left(|L,\downarrow\rangle \pm |R,\downarrow\rangle\right), \tag{S1}$$

which correspond to the spin-conserving qubit operation regime.

In contrast, at the detuning positions $\delta = -\delta_0$ and $\delta = +\delta_0$, avoided crossings occur between opposite-spin states due to the RSOC. These crossings give rise to spin-hybridized superposition states

$$\delta = -\delta_0: \quad |\psi\rangle = \frac{1}{\sqrt{2}}\left(|L,\downarrow\rangle \pm |R,\uparrow\rangle\right), \tag{S2}$$

$$\delta = +\delta_0: \quad |\psi\rangle = \frac{1}{\sqrt{2}}\left(|L,\uparrow\rangle \pm |R,\downarrow\rangle\right), \tag{S3}$$

which serve as the basis states for electrically driven spin-flip qubit manipulations.

These eigenstate visualizations confirm that the qubit operation regimes identified in the detuning spectrum originate from state-selective hybridization between the DQDs, controlled by the combined effect of detuning and RSOC.

Supplementary Materials Section 6. Deformation of tunnel coupling

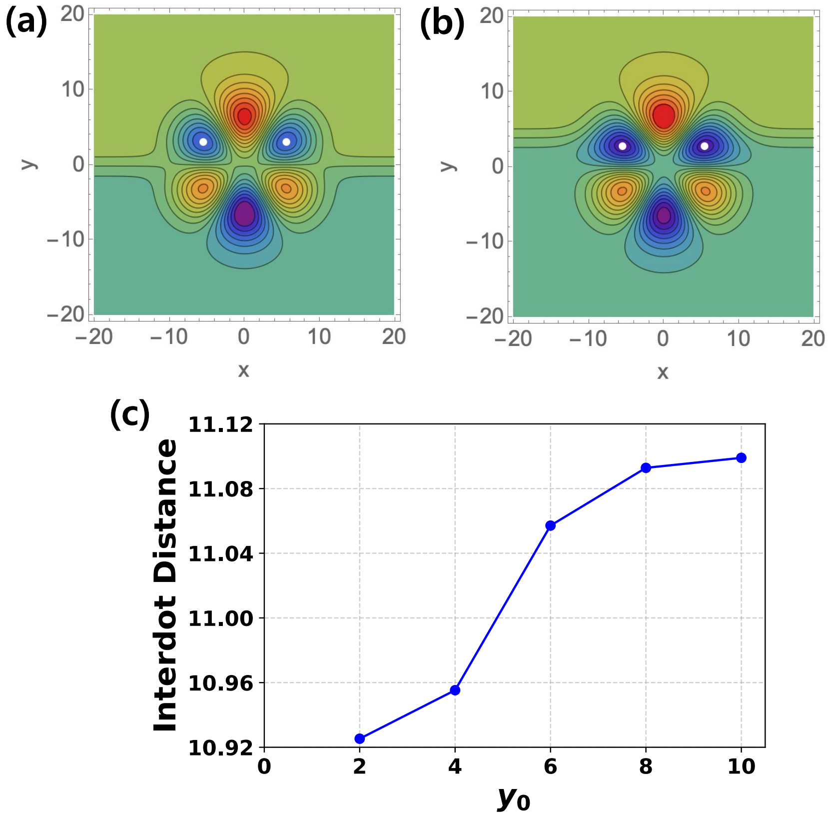

Figure S6: Effective potential landscape and interdot distance as a function of y_0. (a,b) Two-dimensional maps of the effective potential V_{eff} for $y_0 = 0$ (a) and $y_0 = 6$ (b), where y_0 denotes the position of the p-n interface channel. The contour plots illustrate the evolution of the two local potential minima defining the DQDs. (c) Interdot distance between the minimum points of two QDs as a function of y_0.

As mentioned in the main text, the Δ_{sc} is not explicitly related to RSOC. Nevertheless, the gap decreases with increasing RSOC strength, as shown in Fig. 3(b) in the main text. To gain further insight into these gap behaviors, we analyze the gap characteristics using the effective potential. The effective potential is written as Equation (2) in the main text.

Supplementary Figures S6(a) and (b) show how the effective potential landscape evolves as the junction interface position y_0 is shifted. The blue region denotes the confining potential well, and the white dots mark the local minima associated with the two quantum dots. As the interface moves toward positive y, the potential well becomes increasingly deformed, which in turn enlarges the spatial separation between the two local minima. This geometric modification reduces the overlap between the localized wave functions, effectively weakening the interdot coupling.

The consequence of this deformation is quantified in Supplementary Fig. S6(c), where the increasing minimum-to-minimum distance correlates with a reduction in the measured spin-conserving gap Δ_{sc}. Importantly, the intrinsic Δ_{sc} itself is not directly altered by the RSOC strength; rather, the apparent change arises because increasing the RSOC strength induces an effective displacement of the p-n junction interface, which subsequently modifies the DQD confinement potential. In this sense, RSOC tuning mimics the effect of shifting y_0, providing a unified interpretation of how RSOC indirectly influences Δ_{sc} through deformation of the effective potential landscape.

Supplementary Materials Section 7. Kramers degeneracy

To examine the symmetry of the effective Hamiltonian in Eq. (3) in the main text, we express it in terms of Pauli matrices in the basis $\{|L,\uparrow\rangle,\ |L,\downarrow\rangle,\ |R,\uparrow\rangle,\ |R,\downarrow\rangle\}$. The Hamiltonian projected onto this subspace is given by

$$H_K(\delta,\Delta_z,\lambda_R,t_c)=\frac{\alpha\delta}{2}\tau_z\otimes\sigma_0+t_c\tau_x\otimes\sigma_0+\frac{\Delta_z+\gamma\lambda_R^2}{2}\tau_0\otimes\sigma_z+\frac{\beta\lambda_R}{2}\tau_y\otimes\sigma_y, \tag{S4}$$

where τ_i and σ_i denote the Pauli matrices acting on the dot (L/R) and spin subspaces, respectively.

We now examine the time-reversal symmetry (TRS) of this Hamiltonian. The time-reversal operator for spin-1/2 systems is given by

$$\mathcal{T}=I_\tau\otimes(i\sigma_y)K, \tag{S5}$$

where K denotes complex conjugation. Under time reversal, the spin Pauli matrices transform as $\boldsymbol{\sigma}\to-\boldsymbol{\sigma}$, while the orbital (dot) Pauli matrices remain unchanged, $\boldsymbol{\tau}\to\boldsymbol{\tau}$, and $i\to-i$ due to complex conjugation.

The detuning term $\tau_z\otimes\sigma_0$ and the tunneling term $\tau_x\otimes\sigma_0$ are spin-independent and therefore invariant under $\mathcal{T}$. The RSOC term $\tau_y\otimes\sigma_y$ also preserves TRS, since σ_y changes sign under time reversal while τ_y remains unchanged, leaving the product invariant. In contrast, the Zeeman term $\tau_0\otimes\sigma_z$ changes sign under time reversal and therefore breaks TRS. We note that this Hamiltonian describes only a single-valley subspace of the full system, and thus does not by itself need to preserve TRS.

We now consider the Hamiltonian of the total system including both valleys. In the basis $\{|K,L,\uparrow\rangle,\ |K,L,\downarrow\rangle,\ |K,R,\uparrow\rangle,\ |K,R,\downarrow\rangle, |K',L,\uparrow\rangle,\ |K',L,\downarrow\rangle,\ |K',R,\uparrow\rangle,\ |K',R,\downarrow\rangle\}$, and in the absence of intervalley scattering, the Hamiltonian can be written as

$$H_{\mathrm{tot}}=\begin{bmatrix}H_K & 0\\ 0 & H_{K'}\end{bmatrix}, \tag{S6}$$

with

$$H_{K'}(\delta,\Delta_z,\lambda_R,t_c)=\frac{\alpha\delta}{2}\tau_z\otimes\sigma_0+t_c\tau_x\otimes\sigma_0+\frac{\Delta_z-\gamma\lambda_R^2}{2}\tau_0\otimes\sigma_z+\frac{\beta\lambda_R}{2}\tau_y\otimes\sigma_y. \tag{S7}$$

To describe the full system in a compact form, we introduce the Pauli matrices ν_i acting in the valley subspace. In the basis $(K,K')\otimes(L,R)\otimes(\uparrow,\downarrow)$, the total Hamiltonian is written as

$$H_{\mathrm{tot}}=\frac{\alpha\delta}{2}\nu_0\otimes\tau_z\otimes\sigma_0+t_c\nu_0\otimes\tau_x\otimes\sigma_0+\frac{\Delta_z}{2}\nu_0\otimes\tau_0\otimes\sigma_z+\frac{\gamma\lambda_R^2}{2}\nu_z\otimes\tau_0\otimes\sigma_z+\frac{\beta\lambda_R}{2}\nu_0\otimes\tau_y\otimes\sigma_y, \tag{S8}$$

where ν_i are Pauli matrices acting in the valley subspace. The second-order Rashba-induced term is valley-odd, whereas the other terms are valley-even.

Under time reversal, the spin Pauli matrices transform as $\boldsymbol{\sigma}\to-\boldsymbol{\sigma}$, while the valley index is exchanged ($K\leftrightarrow K'$), corresponding to $\nu_z\to-\nu_z$. As a result, the valley-odd term $\nu_z\otimes\sigma_z$ remains invariant under TRS, whereas the Zeeman term σ_z changes sign. Therefore, the total Hamiltonian preserves TRS only when $\Delta_z=0$, while any finite Zeeman field explicitly breaks TRS.

Supplementary Materials Section 8. The effective 4-bands Hamiltonian of our device model

Second-order term of RSOC

We note that the Rashba term does not directly split the spin states at first order but generates a second-order virtual energy shift, $\delta E \sim \gamma\lambda_R^2$, which appears as a Zeeman-like correction after projection onto the low-energy sector.

We decompose the Hamiltonian of Eq. (S4) into an unperturbed part and a perturbation as

$$H = H_0 + V \tag{S9}$$

where

$$\begin{aligned} H_0 &= \tfrac{\alpha\delta}{2}\tau_z + t_c\tau_x, \\ V &= \tfrac{\Delta_z}{2}\sigma_z \end{aligned} \tag{S10}$$

The eigenstates of H_0 are written by $|s,\eta\rangle$, with corresponding eigenenergies

$$E^{(0)}_{s,\eta} = s\Omega + \eta\frac{\Delta_z}{2} \tag{S11}$$

where $s = \pm 1$ labels the isospin (bonding/antibonding), $\eta = \pm 1$ denotes the spin, and

$$\Omega = \sqrt{(\frac{\alpha\delta}{2})^2 + t_c^2}. \tag{S12}$$

The first-order correction vanishes because the perturbation $V \propto \tau_y\sigma_y$ flips both the orbital and spin indices. Therefore, it does not couple a state to itself but only connects it to orthogonal states, leading to a zero diagonal matrix element,

$$E^{(1)}_{s,\eta} = \langle s,\eta|V|s,\eta\rangle, \tag{S13}$$

since both τ_y and σ_y are purely off-diagonal in their respective eigenbases.

Using standard nondegenerate perturbation theory, the second-order energy correction is given by

$$E^{(2)}_{s,\eta} = \sum_{(s',\eta')\neq(s,\eta)} \frac{|\langle s',\eta'|V|s,\eta\rangle|^2}{E^{(0)}_{s,\eta} - E^{(0)}_{s',\eta'}}. \tag{S14}$$

Since the perturbation $V = (\beta\lambda_R/2)\tau_y\sigma_y$ flips both the isospin and spin indices, the only nonzero matrix element connects $|s,\eta\rangle$ to $|-s,-\eta\rangle$. Thus, the summation reduces to a single term, yielding

$$E^{(2)}_{s,\eta} = \frac{(\frac{\beta\lambda_R}{2})^2}{E^{(0)}_{s,\eta} - E^{(0)}_{s',\eta'}}. \tag{S15}$$

Evaluating the denominator explicitly, we obtain

$$E^{(0)}_{s,\eta} - E^{(0)}_{s',\eta'} = 2s\Omega + \eta\Delta_z. \tag{S16}$$

Therefore, the second-order correction takes the form

$$E^{(2)}_{s,\eta} = \frac{(\frac{\beta\lambda_R}{2})^2}{2s\Omega + \eta\Delta_z}. \tag{S17}$$

This result shows that the RSOC does not contribute at first order. As shown in Eq. (S14), the second-order process returns the system to its initial state through two successive perturbations, resulting in a diagonal energy renormalization via virtual spin-flip and interdot transitions. This mechanism is consistent with previous studies, where RSOC induces mixing of spin states and leads to level anticrossing through higher-order processes [6, 7].

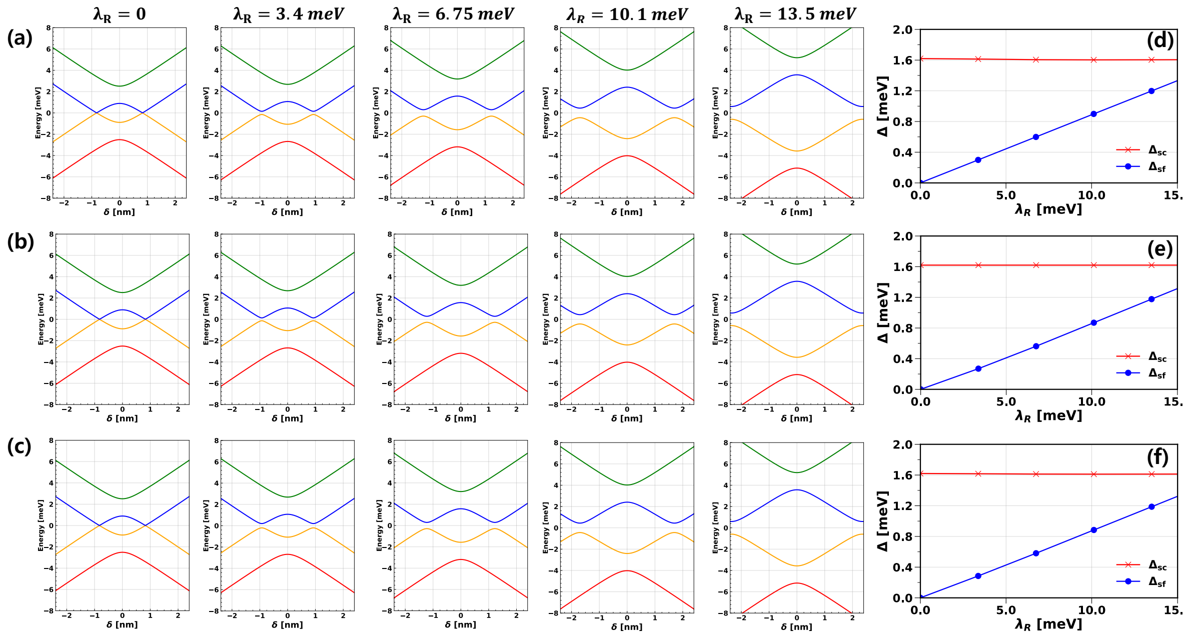

Figure S7: Comparison of effective-model fittings and gap evolutions for different RSOC coupling structures in the four-band Hamiltonian. Effective-model spectra generated using (a) the $\tau_y\sigma_y$ RSOC term, (b) the $\tau_x\sigma_y$ RSOC term, and (c) both coupling terms simultaneously. (d-f) Gap evolutions as a function of λ_R at fixed Δ_z, corresponding to (a), (b), and (c), respectively.

TRS analysis of the RSOC-induced coupling

To further examine the form of the RSOC-induced coupling in the projected four-band Hamiltonian, we compared effective models containing (i) the $\tau_y\sigma_y$ term, (ii) the $\tau_x\sigma_y$ term, and (iii) both coupling terms simultaneously. As shown in Fig. S7, all three models reproduce qualitatively similar detuning spectra and gap evolutions. Therefore, the choice of the minimal coupling term should additionally be guided by the symmetry properties of the projected low-energy model.

Since RSOC arises from relativistic spin-orbit interaction associated with inversion-symmetry breaking rather than magnetic ordering, the RSOC-induced coupling should remain compatible with the effective time-reversal-symmetric structure of the zero-field projected Hamiltonian. As discussed in Supplementary Materials Section 7, under the time-reversal operation $T = \tau_0 \otimes i\sigma_y K$, the spin Pauli matrix changes sign, $\sigma_y \to -\sigma_y$, while τ_y also changes sign because it is purely imaginary. Consequently, the product $\tau_y\sigma_y$ remains invariant under time reversal and preserves the zero-field degeneracy structure of the projected model. In contrast, a B-independent $\tau_x\sigma_y$ term is odd under time reversal within the projected low-energy model, because τ_x remains unchanged whereas σ_y changes sign under the time-reversal operation. Such a term would therefore explicitly break the effective time-reversal-symmetric structure of the zero-field Hamiltonian. We therefore adopt the $\tau_y\sigma_y$ term as the minimal symmetry-compatible representation of the RSOC-induced spin-flip coupling in our projected four-band Hamiltonian.

Full matrix form of effective 4-bands Hamiltonian

The full matrix representation of Eq. (S4) is given by

$$H = \begin{bmatrix} \frac{\alpha\delta}{2} + \frac{1}{2}\left(\Delta_z + \gamma\lambda_R^2\right) & 0 & t_c & -\frac{1}{2}\beta\lambda_R \\ 0 & \frac{\alpha\delta}{2} - \frac{1}{2}\left(+\Delta_z + \gamma\lambda_R^2\right) & \frac{1}{2}\beta\lambda_R & t_c \\ t_c & \frac{1}{2}\beta\lambda_R & -\frac{\alpha\delta}{2} + \frac{1}{2}\left(\Delta_z + \gamma\lambda_R^2\right) & 0 \\ -\frac{1}{2}\beta\lambda_R & t_c & 0 & -\frac{\alpha\delta}{2} - \frac{1}{2}\left(+\Delta_z + \gamma\lambda_R^2\right) \end{bmatrix}$$

By fitting to the result of our tight-binding numerical simulation, we obtained the following parameters in the effective Hamiltonian: $t_c = 0.3$, $\Delta_z = 1.26$, $\lambda = 2n \times \Delta_z$ (n=integer), $\alpha = 0.33$, $\beta = 0.022$, and $\gamma = 0.0048$.

This effective four-band Hamiltonian enables us to analyze the evolution of the characteristic energy gaps systematically. In particular, we focus on the spin-conserving gap, the spin-flip gap, and their dependence on the key parameters. Specifically, we investigate how the gaps evolve as functions of Zeeman energy, RSOC strength, detuning, and interdot coupling. Supplementary Figure S4(b) presents the energy spectrum as a function of detuning, which corresponds to the same behavior shown in Supplementary Fig. S4(a). From these spectra, we extracted the gap evolution using Eq. (S4), and the results are summarized in Supplementary Figure S7(d). The trend obtained by our effective four-band Hamiltonian is consistent with the numerical simulation results shown in Fig. 3(b) in the main text, confirming the validity of our four-band model.

Supplementary Materials Section 9. Intervalley scattering

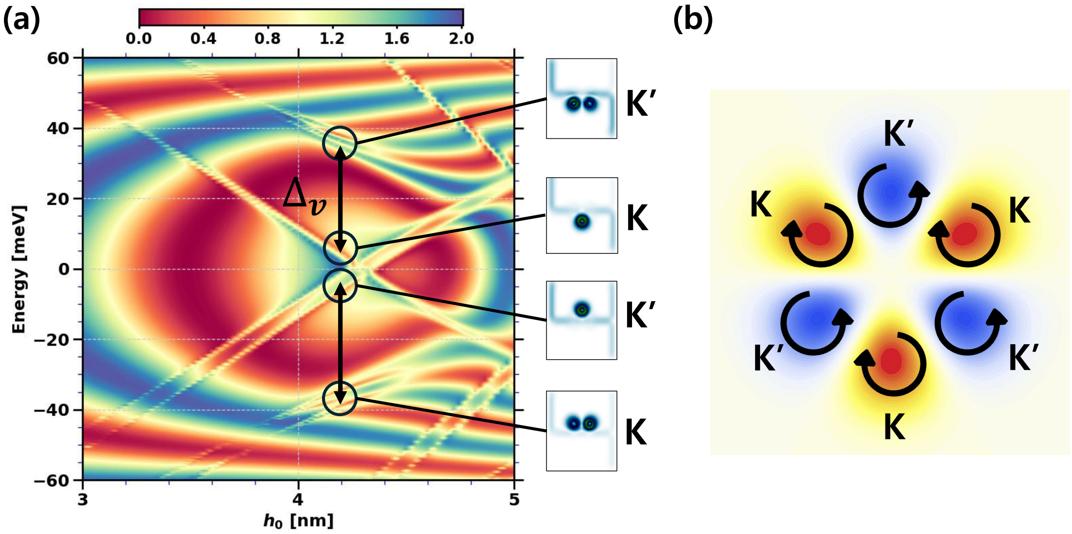

Figure S8: (a) Quantum conductance map as a function of nanobubble height h_0 and energy, with the corresponding current density distribution at selected Fano resonance lines shown on the right. Δ_v indicates the energy splitting between K and K' valley. (b) Schematic illustration of valley-dependent cyclotron motion induced by PMF.

Intervalley scattering in graphene requires a large momentum transfer on the order of $|K - K'|$, which can only be induced by atomically sharp disorder or short-range potentials. In contrast, the smoothly varying p-n junction and Gaussian-shaped nanobubble considered in our system do not provide such momentum transfer, thereby suppressing intervalley mixing. Without spin degrees of freedom [2], the intervalley splitting Δ_v is approximately 40 meV, which is significantly larger than the relevant energy scales considered in our model, including the RSOC ($\lambda_R \sim 10.1\ meV$) and the Zeeman energy ($\Delta_z \sim 1.7\ meV$). As a result, the qubit defined within a single valley is not affected by the opposite PMF in the other valley, and its coherence properties are expected to remain robust. Therefore, valley mixing is negligible in our system, justifying the single-valley description used throughout this work.

Supplementary Materials Section 10. Calculation Methods

Strain-induced Nanobubble

The nanobubble is assumed to follow a Gaussian profile, which describes the out-of-plane displacement field,

$$z(r) = h_0 \exp\left(-\frac{r^2}{2\sigma^2}\right), \tag{S18}$$

where h_0 denotes the maximum height of the bubble and σ characterizes its lateral width. In this study, we use $h_0 = 4.29$ nm and $\sigma = 7.38$ nm. Such nanobubbles are commonly observed in graphene placed on a substrate, arising from trapped molecules or strain relaxation [8–14]. Local strain in nanobubbles naturally generates PMFs, which confine Dirac fermions and lead to the formation of localized quantum states, effectively acting as single- and double-quantum-dot states, as shown in Fig. 1(a) of the main text. To probe and manipulate these quantum-dot-like states, we place the nanobubble at the interface of a graphene p-n junction. In the quantum Hall regime, the p-n junction hosts chiral interface channels, which can couple to the localized states in the strained region. This coupling realizes a hybrid system, where quantum Hall edge currents interact with the PMF-generated quantum dots, forming a controllable two-level system (TLS) suitable for qubit operations.

Quantum Transport

The transport properties are computed within the Landauer-Büttiker formalism. The conductance at energy E is given by

$$G(E) = \frac{2e^2}{h} T_{\alpha\beta}(E), \tag{S19}$$

where $T_{\alpha\beta}(E)$ is the transmission probability from lead β to lead α. This transmission is obtained from the scattering matrix S of the system,

$$T_{\alpha\beta}(E) = \sum_{n\in\alpha, m\in\beta} \left|S_{nm}(E)\right|^2, \tag{S20}$$

with propagating modes labeled n_α and m_β in the corresponding leads. In our model, spin degeneracy is explicitly included so that the conductance spectra exhibit quantized steps in units of e^2/h per total spin channel. This allows us to resolve the interplay between spin splitting, Rashba coupling, and pseudomagnetic confinement in the proposed nanobubble-based spin qubit system.

Rabi Oscillations

Basis of the Four-band Hamiltonian

Following the localized basis defined in Fig. 3(a) of the main text,

$$\{|L,\uparrow\rangle,\ |L,\downarrow\rangle,\ |R,\uparrow\rangle,\ |R,\downarrow\rangle\},$$

we use the four-band Hamiltonian given in Eq. (3) of the main text to perform Rabi oscillations. As shown in the energy spectra in Supplementary Fig. S4, the detuning parameter δ controls the electrostatic offset between the two dots and thereby drives the transitions at the relevant avoided crossings. As discussed in Sec. 2.3 of the main text, these avoided crossings fall into two categories: spin-conserving and spin-flip transitions.

Identification of the avoided crossings

For each detuning value δ, we compute the four eigenvalues of Eq. (3) of the main text, ordered as

$$E_1(\delta) \leq E_2(\delta) \leq E_3(\delta) \leq E_4(\delta).$$

▶ **spin-conserving avoided crossing.** This avoided crossing corresponds to the upper pair of eigenvalues. The gap is defined as

$$\Delta_{\mathrm{sc}}(\delta) = E_4(\delta) - E_3(\delta), \tag{S21}$$

and occurs at $\delta = 0$ for our model parameters.

▶ **spin-flip avoided crossing.** The Rashba spin-orbit-mediated avoided crossing involves the middle pair of eigenvalues, with the gap

$$\Delta_{\mathrm{sf}}(\delta) = E_3(\delta) - E_2(\delta). \tag{S22}$$

The detuning point $\delta_0 < 0$ is obtained by minimizing $\Delta_{\mathrm{sf}}(\delta)$ over negative δ.

These avoided crossings define the relevant two-level subspaces for the Rabi-map simulations.

Observables for the two interdot transitions

Detuning controls two distinct interdot transitions in the DQD, as explained in Section 2.3 in the main text. Because the two transitions involve different pairs of states, we employ different observables for the dynamics.

▶ **spin-conserving interdot transition.** When both participating states share the same spin orientation (e.g., $|L,\uparrow\rangle$ and $|R,\uparrow\rangle$), detuning induces an interdot charge transfer without flipping the spin as shown in Fig. 1(c) of the main text. The appropriate observable is

$$\tau_z = (|L,\uparrow\rangle\langle L,\uparrow| + |L,\downarrow\rangle\langle L,\downarrow|) - (|R,\uparrow\rangle\langle R,\uparrow| + |R,\downarrow\rangle\langle R,\downarrow|). \tag{S23}$$

This quantity measures the left-right charge transfer and corresponds to the observable denoted as $\langle\tau_z\rangle$ in Figs. 4(a), (c), and (e) of the main text.

▶ **spin-flip interdot transition.** The spin-flip transition occurs between $|L,\downarrow\rangle$ and $|R,\uparrow\rangle$, where spin-orbit coupling mediates a combined interdot tunneling between different spin orientations as shown in Fig. 1(d) of the main text. To capture this process, we use the population difference between the two states forming the avoided crossing,

$$\sigma_z = |L,\downarrow\rangle\langle L,\downarrow| - |R,\uparrow\rangle\langle R,\uparrow|. \tag{S24}$$

This observable captures the spin-orbit-assisted interdot transition and is labeled $\langle\sigma_z\rangle$ in Figs. 4(b), (d), and (f) of the main text.

Liouvillian time evolution

The density matrix obeys the Lindblad master equation

$$\frac{d\rho}{dt} = -i[H,\rho] + \sum_k (L_k^\dagger \rho L_k - \frac{1}{2}\{(L_k^\dagger L_k, \rho\}. \tag{S25}$$

Relaxation and dephasing within the two-level subspace are included through the collapse operators

$$\Gamma_1 = \sqrt{1/T_1}\,|g\rangle\langle e|, \qquad \Gamma_\phi = \sqrt{1/T_2 - 1/(2T_1)}\,(|e\rangle\langle e| - |g\rangle\langle g|)\,, \tag{S26}$$

where $|e\rangle$ and $|g\rangle$ denote the relevant pair of states for each type of interdot transition.

We solve the master equation $\dot\rho = L\rho$ by computing the exponential action $e^{Lt}|\rho(0)\rangle$ using a Krylov subspace method.

Rabi-map construction

For each detuning offset, we compute the observable expectation value using the vec-trace identity,

$$\langle O(t)\rangle = \mathrm{Tr}[O\rho(t)] = \mathrm{vec}(O^T)^\dagger \, |\rho(t)\rangle\rangle, \tag{S27}$$

with $O = \tau_z$ for the spin-conserving transition and $O = \sigma_z$ for the spin-flip transition.

Repeating this calculation over a two-dimensional grid of detuning and time produces the Rabi maps presented in Fig. 4 of the main text. In addition, in our Rabi-oscillation simulations, we took $T_1 = 750$ ps, the maximum relaxation time obtained from the detuning-energy spectra in Fig. S4(a). Because the dephasing time must satisfy $2T_2 \leq T_1$, we used $T_2 = T_1/2$ in our calculation.

As we mentioned in Supplementary Materials Section 4, relaxation time is extracted from the detuning-dependent energy spectrum by identifying spin-conserving and spin-flip transition points where Fano resonances emerge. From the linewidth of these resonances, we determine an effective relaxation timescale. We emphasize that this T_1 does not represent the intrinsic coherence limit of graphene, but rather serves as an effective parameter describing environment-induced dissipation, allowing us to investigate the Rabi dynamics within a relevant operational regime.

Furthermore, as shown in Fig. 4 of the Supplementary Materials of Ref. [2], increasing the junction width ξ leads to more pronounced and eventually saturated resonance peaks near $E \approx \pm 0.04$, accompanied by a clear narrowing of their linewidths. This behavior indicates that in smoother and more realistic potential profiles, the effective dissipation rate is reduced, corresponding to an increase in the relaxation time. While a quantitatively accurate determination of relaxation times would require a more detailed treatment of environmental coupling and noise, which is beyond the scope of this work, our results demonstrate that the proposed device operates within a physically reasonable regime and highlight its potential as a viable spin-qubit platform.

References

[1] N. Myoung and H. C. Park, *Conductance oscillations in chern insulator junctions: Valley-isospin dependence and aharonov-bohm effects*, Phys. Rev. B **96** (2017) 235435.

[2] N. Myoung, H. Choi, and H. C. Park, *Manipulation of valley isospins in strained graphene for valleytronics*, Carbon **157** (2020) 578.

[3] H. C. Park, J. Han, and N. Myoung, *A strain-engineered graphene qubit in a nanobubble*, Quantum Science and Technology **8** (2023) 025012.

[4] M.-H. Liu *et al.*, *Scalable tight-binding model for graphene*, Phys. Rev. Lett. **114** (2015) 036601.

[5] M.-H. Liu *et al.*, *Scalable tight-binding model for strained graphene*, `arXiv:2603.02077`.

[6] D. V. Bulaev and D. Loss, *Spin relaxation and anticrossing in quantum dots: Rashba versus dresselhaus spin-orbit coupling*, Phys. Rev. B **71** (2005) 205324.

[7] P. Stano, *Controlling electron quantum dot qubits by spin-orbit interactions*, PhD., dissertation submitted to Universität Regensburg (2007) .

[8] P. Jia *et al.*, *Programmable graphene nanobubbles with three-fold symmetric pseudo-magnetic fields*, Nature Communications **10** (2019) 3127.

[9] H. Ghorbanfekr-Kalashami, K. S. Vasu, R. R. Nair, F. M. Peeters, and M. Neek-Amal, *Dependence of the shape of graphene nanobubbles on trapped substance*, Nature Communications **8** (2017) 15844.

[10] G. Zamborlini *et al.*, *Nanobubbles at gpa pressure under graphene*, Nano Letters **15** (2015) 6162.

[11] F. Faraji, M. Neek-Amal, E. C. Neyts, and F. M. Peeters, *Indentation of graphene nano-bubbles*, Nanoscale **14** (2022) 5876.

[12] R. Villarreal *et al.*, *Breakdown of universal scaling for nanometer-sized bubbles in graphene*, Nano Letters **21** (2021) 8103.

[13] N. N. Klimov *et al.*, *Electromechanical properties of graphene drumheads*, Science **336** (2012) 1557.

[14] S. Zhu *et al.*, *Pseudomagnetic fields in a locally strained graphene drumhead*, Phys. Rev. B **90** (2014) 075426.